ϕ_m (Fig. 1d). Figure 1d shows a plot of the concentration of the particles that arrived at the surface of the electrode (in terms of the fraction of the occupied area) against the frequency of the applied field. Therefore the supersaturation can be determined from Fig. 1d.

Identification of crystalline nuclei

We used two criteria to identify the crystalline nuclei in the process of nucleation of colloidal particles. (1) Two particles were defined as neighbours if the centre-to-centre distance between them was smaller than a cut-off value of 1.80*a*, chosen to be close to the minimum between the first and second peaks of the PCF $g(r)$ for our samples (Fig. 1c). (2) A particle was defined as a member of a 2D crystal if it had more than two neighbours. To exclude the structures of circles or dumbbells (two crystals linked with a long chain) and to consider the structural relaxation, we further confined the bond angles between a particle and its neighbours to $\pi/3 \pm \pi/12$, which corresponds to the deviation from the six-fold symmetric bond angle.

Received 23 November 2003; accepted 10 May 2004; doi:10.1038/nature02630.

1. Sato, K., Furukawa, Y. & Nakajima, K. (eds) *Advances in Crystal Growth* (Elsevier Science, Amsterdam, 2001).
2. Abraham, F. F. *Homogeneous Nucleation Theory* (Academic, New York, 1974).
3. Kashchiev, D. *Nucleation: Basic Theory with Applications* (Butterworth-Heinemann, Oxford, 2000).
4. Laaksonen, A., Talanquer, V. & Oxtoby, D. W. Nucleation: Measurements, theory, and atmospheric applications. *Annu. Rev. Phys. Chem.* **46,** 489–524 (1995).
5. Chernov, A. A. *Modern Crystallography III—Crystal Growth* (Springer, Berlin, 1984).
6. Skripov, V. P. in *Current Topics in Materials Science* Vol. 2 (ed. Kaldis, E.) 328–378 (North-Holland, Amsterdam, 1981).
7. McGraw, R. & Laaksonen, A. Scaling properties of the critical nucleus in classical and molecular-based theories of vapor-liquid nucleation. *Phys. Rev. Lett.* **76,** 2754–2757 (1996).
8. Trau, M., Saville, D. A. & Aksay, I. A. Field-induced layering of colloidal crystals. *Science* **272,** 706–709 (1996).
9. Palberg, T. Crystallization kinetics of repulsive colloidal spheres. *J. Phys. Condens. Matter* **11,** R323–R360 (1999).
10. Larsen, A. E. & Grier, D. G. Like-charge attractions in metastable colloidal crystallites. *Nature* **385,** 230–233 (1997).
11. Yethiraj, A. & van Blaaderen, A. A colloidal model system with an interaction tunable from hard spheres to soft and dipolar. *Nature* **421,** 513–517 (2003).
12. Pusey, P. N. in *Liquids, Freezing and the Glass Transition* (eds Leveesque, D., Hansen, J. P. & Zinn-Justin, J.) Ch. 5 (Elsevier, Amsterdam, 1991).
13. Gasser, U., Weeks, E. R., Schofield, A., Pusey, P. N. & Weitz, D. A. Real-space imaging of nucleation and growth in colloidal crystallization. *Science* **292,** 258–262 (2001).
14. Lucadamo, G. & Medlin, D. L. Geometric origin of hexagonal close packing at a grain boundary in gold. *Science* **300,** 1272–1275 (2003).
15. Caccluto, A., Auer, S. & Frenkel, D. Onset of heterogeneous crystal nucleation in colloidal suspensions. *Nature* **428,** 404–406 (2004).
16. Lumsdon, S. O., Kaler, E. W., Williams, J. P. & Velev, O. D. Dielectrophoretic assembly of oriented and switchable two-dimensional photonic crystals. *Appl. Phys. Lett.* **82,** 949–951 (2003).
17. Norris, D. J. & Vlasov, Y. A. Chemical approaches to three-dimensional semiconductor photonic crystals. *Adv. Mater.* **13,** 371–376 (2001).
18. Kumacheva, E., Golding, R. K., Allard, M. & Sargent, E. H. Colloid crystal growth on mesoscopically patterned surfaces: effect of confinement. *Adv. Mater.* **14,** 221–224 (2002).
19. Pan, G. S., Kesmamoothy, R. & Asher, S. A. Optically nonlinear Bragg diffracting nanosecond optical switches. *Phys. Rev. Lett.* **78,** 3860–3863 (1997).
20. Khopade, A. J. & Caruso, F. Stepwise self-assembled poly(amidoamine) dendrimer and poly(styrenesulfonate) microcapsules as sustained delivery vehicles. *Biomacromolecules* **3,** 1154–1162 (2002).
21. Velev, O. D. & Kaler, E. W. In situ assembly of colloidal particles into miniaturized biosensors. *Langmuir* **15,** 3693–3698 (1999).
22. Fowler, R. & Giggenhein, E. A. *Statistical Thermodynamics* (Cambridge Univ. Press, London, 1960).
23. Yeh, S. R., Seul, M. & Shraiman, B. I. Assembly of ordered colloidal aggregates by electric-field-induced fluid flow. *Nature* **386,** 57–59 (1997).
24. Stiles, P. J. & Regan, H. M. Transient cellular convection in electrically polarized colloidal suspensions. *J. Colloid Interface Sci.* **202,** 562–565 (1998).
25. Trau, M., Sankaran, S., Saville, D. A. & Aksay, A. I. Electric-field-induced pattern formation in colloidal suspensions. *Nature* **374,** 437–439 (1995).
26. Crocker, J. C. & Grier, D. G. Methods of digital video microscopy for colloidal studies. *J. Colloid Interface Sci.* **179,** 298–310 (1996).
27. Liu, X. Y. in *Advances in Crystal Growth Research* (eds Sato, K., Nakajima, K. & Furukawa, Y.) 42–61 (Elsevier Science, Amsterdam, 2001).
28. Liu, X. Y., Maiwa, K. & Tsukamoto, K. Heterogeneous two-dimensional nucleation and growth kinetics. *J. Chem. Phys.* **106,** 1870–1879 (1997).
29. Auer, S. & Frenkel, D. Line tension controls wall-induced crystal nucleation in hard-sphere colloids. *Phys. Rev. Lett.* **91,** 015703 (2003).
30. Bowles, R. K. *et al.* A molecular based derivation of the nucleation theorem. *J. Chem. Phys.* **113,** 4524–4532 (2000).

Supplementary Information accompanies the paper on **www.nature.com/nature**.

Acknowledgements We thank D.W. Li for help with the imaging process, and for discussions. We also thank C. Strom for reading the draft. This work was supported by the Science and Engineering Research Council of Singapore.

Competing interests statement The authors declare competing financial interests: details accompany the paper on **www.nature.com/nature**.

Correspondence and requests for materials should be addressed to X.Y.L. (phyliuxy@nus.edu.sg).

The influence of ridge migration on the magmatic segmentation of mid-ocean ridges

S. M. Carbotte, C. Small & K. Donnelly

Lamont-Doherty Earth Observatory, 61 Rte 9W, Palisades, New York 10964, USA

The Earth's mid-ocean ridges display systematic changes in depth and shape, which subdivide the ridges into discrete spreading segments bounded by transform faults and smaller non-transform offsets of the axis[1–3]. These morphological changes have been attributed to spatial variations in the supply of magma from the mantle, although the origin of the variations is poorly understood[1,4,5]. Here we show that magmatic segmentation of ridges with fast and intermediate spreading rates is directly related to the migration velocity of the spreading axis over the mantle. For over 9,500 km of mid-ocean ridge examined, leading ridge segments in the 'hotspot' reference frame coincide with the shallow magmatically robust segments across 86 per cent of all transform faults and 73 per cent of all second-order discontinuities. We attribute this relationship to asymmetric mantle upwelling and melt production due to ridge migration, with focusing of melt towards ridge segments across discontinuities. The model is consistent with variations in crustal structure across discontinuities of the East Pacific Rise, and may explain variations in depth of melting and the distribution of enriched lavas.

Changes in the elevation and cross-axis morphology of a mid-ocean ridge (MOR) often coincide with differences in crustal indicators of magmatic activity, such as the age and composition of axial lavas, presence of crustal magma bodies, and extent of crustal fracturing[6–8]. These correlations have led to the hypothesis that the morphology of a spreading centre is an indicator of the distribution and delivery of magma from the mantle, with shallow and broad ridge segments believed to reflect enhanced magma supply, whereas deeper, more tectonized segments are magma-starved[1,9]. Although magmatic segmentation is widely accepted as a fundamental characteristic of a MOR, the significance of this segmentation for the pattern of mantle upwelling is actively debated, particularly for fast-spreading ridges[4,5,10,11].

Our analysis of elevation changes along MORs in the context of absolute plate motions reveals a remarkably consistent relationship between magmatic segmentation inferred from ridge morphology and absolute migration velocity of the spreading centre. Plate boundaries migrate at a rate and direction determined by the absolute motions of the bounding plates[12]. Currently, all spreading centres are migrating relative to the 'fixed' hotspot reference frame[13]. Along the fast spreading northern East Pacific Rise (NEPR), the spreading centre migrates to the northwest with minor changes in rate and direction along the ridge axis (Fig. 1). Depth profiles along the spreading axis show that shallow ridge segments are consistently offset in the direction of ridge migration relative to the deeper adjacent segments. For the roughly 2,000 km of the NEPR examined (3° to 23° N), this relationship is observed at all transform faults, as well as 6 out of 7 overlapping spreading centres (OSCs) classified as second-order discontinuities (following ref. 1). Analysis of other fast- and intermediate-spreading ridges, encompassing roughly one-fifth of the world's MORs, reveals steps in axial depth consistent with the direction of ridge migration at 86% of transform faults and 73% of second-order discontinuities (Fig. 2, Supplementary Figs 1 and 2).

Steps in ridge elevation across discontinuities, which are ubiqui-

tous along MORs, can not be attributed to cooling related to juxtaposition of older lithosphere across a ridge offset, as this thermal edge effect is expected to affect both segments on either side of a discontinuity equally. Furthermore, thermal edge effects should be smaller at second-order discontinuities where the lithospheric age contrast across the offset is minor (~0.1–1 Myr). Instead, elevation changes observed at both non-transform and transform offsets span a similar wide range (10 to ~500 m), although there is an order of magnitude difference in offset length (typically >50 km for transform faults compared with 5–20 km for non-transform offsets; Fig. 2). Where leading segments are shallower, depth anomalies across discontinuities vary with offset length, with the largest depth anomalies found at offsets of less than ~150 km and smaller anomalies at longer transform faults (Fig. 2). In contrast, for the few cases where trailing segments are shallower, depth changes are typically small (<100 m) and there is no trend with ridge offset length.

Why do the leading segments along these MORs overwhelmingly correspond with the shallower, morphologically robust segments? We suggest that these variations in ridge morphology may result from melt focusing across discontinuities from a broad asymmetric zone of mantle upwelling associated with migrating spreading centres. Kinematic models of passive plate-driven upwelling beneath a migrating MOR predict significant asymmetries in mantle flow paths, with faster mantle upwelling and greater melt production beneath an advancing plate[14,15]. If these models are correct, differences in the mantle flow field and melt production region across discontinuities are expected as a function of the geometry of ridge offset (Fig. 3).

Seismic and seafloor observations indicate that crustal formation occurs within a narrow zone (1–2 km), and melts within the mantle must be strongly focused to the ridge axis. In the case of a segmented spreading centre, focusing of melts may occur not only from the mantle upwelling zone beneath each ridge segment but also from

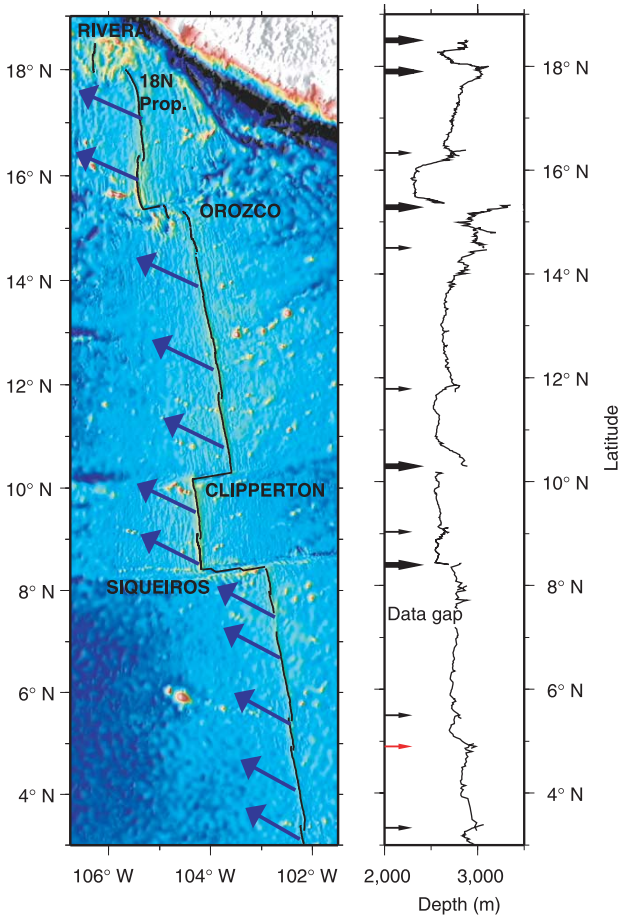

Figure 1 Bathymetry map and axial depth profile along the NEPR. Blue arrows on bathymetry map (left panel) show ridge migration direction calculated from absolute plate motion model HS3-Nuvel1a[28]. Arrow length is proportional to migration rate (1 cm = 55 mm yr^{-1}). Changes in axial depth (right panel) occur at all first-order discontinuities (thick arrows) and smaller offset second-order discontinuities (thin arrows). With one exception (red arrow), ridge segments offset in the direction of ridge migration are shallower. Differences in ridge elevation can persist for all (for example, south of Siqueiros transform fault) or part (for example, north of Clipperton transform fault) of an adjacent ridge segment. 18N Prop., 18° N Propagator.

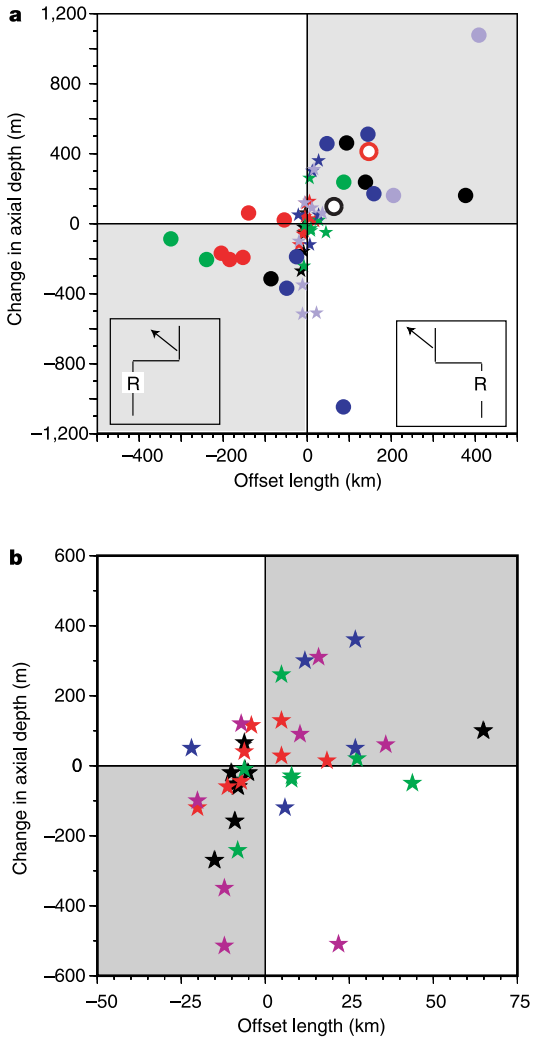

Figure 2 Change in axial depth verses offset length at ridge-axis discontinuities. Change in axial depth is measured as the difference in seafloor depth averaged over a 1-km length of the ridge axis located a uniform distance of 10 km on either side of a discontinuity. Positive axial depth change corresponds to the case where the ridge axis opposite an observer on the spreading axis at R (inset) is shallower. Positive offset length corresponds to the case where the ridge axis steps in the direction of ridge migration relative to observer at R. Grey shading highlights quadrants for which the leading ridge segments are shallower (see text). **a**, Data set includes all transform faults (filled circles), propagating ridge discontinuities (open circles) and non-transform second-order discontinuities (offsets >5 km) along the fast-spreading SEPR from 0°–23° S, 28°–32° S (red), NEPR 3°–23° N (black), Pacific-Antarctic East Pacific Rise 36°–56° S (green), and the intermediate spreading Juan de Fuca-Gorda (purple) and South East Indian ridges 100°–116° E (blue). Bathymetry data used in analysis are from the Ridge Multibeam Synthesis (http://data.ridge2000.org/bathy). **b**, Magnified view showing only the smaller-offset second-order discontinuities.

across ridge-axis discontinuities (see, for example, ref. 16). Indeed, melt may be preferentially entrained across discontinuities where horizontal flow paths are shorter to the adjacent ridge axis, leading to extraction of melts at one segment that originated in the upwelling zone of the neighbouring segment. In the case of a migrating spreading centre, melt focusing towards a leading ridge segment will draw primarily from the faster-upwelling, more melt-rich zone of an advancing plate. In contrast, near the ends of trailing segments, the idealized mantle volume that can be tapped for melt lies primarily within the less melt-rich, slower-upwelling zone of a trailing plate (Fig. 3). In this way, trailing segments lie within the wake or shadow zone of a leading segment, potentially entraining a smaller fraction of the melt generated in the upwelling zone of the adjacent leading segment.

The observations suggest that morphological contrasts between adjacent segments can extend for all or part of a ridge segment, with more persistent differences across transform faults (for example, see Fig. 1). The length of this morphological shadow may reflect the volume of melt tapping from an adjacent upwelling zone, although melt redistribution at crustal levels (for example, through dykes or flow within crustal magma bodies) is likely to be important and would obscure such effects.

The strong correlation between ridge migration direction and contrasts in ridge-axis morphology at OSCs along the East Pacific Rise is surprising, given the small scale of these features (Figs 1, 2b). However, with the overlapping geometry of these offsets, the trailing limb of an OSC will lie within the wake of the leading limb along its entire length (Fig. 3). More melt may be entrained (presumably from shallow levels) by the leading OSC limb as a consequence of enhanced melt production beneath advancing plates. Seismic studies of the 9° 03′ N OSC[17] suggest that melt at crustal levels is fed to the trailing limb of this OSC from the western, advancing-plate side of the discontinuity, consistent with this model. An unusually broad westward dipping magma body underlies the trailing limb of the OSC at the northern end of the overlap zone. Further south, small melt channels are imaged along the western edge of this magma lens, suggesting melt feeding from the west.

Our model for the correlation between ridge segment morphology and ridge migration predicts differences in crustal and upper-mantle structure, which can be tested with seismic and gravity studies and explored with numerical experiments. The model requires upper-mantle flow to be asymmetric beneath migrating MORs, and predicts thicker crust at leading segments. The MELT experiment reveals that mantle structure beneath the southern East Pacific Rise (SEPR) from 15° to 19° S is highly asymmetric, with higher inferred melt contents and stronger upper-mantle anisotropy suggesting greater flow-induced strain beneath the advancing Pacific plate[18–20]. Westward migration of the SEPR has been considered to account for these observations, although existing numerical studies suggest that ridge migration alone is insufficient to explain the large asymmetries observed[21,22]. New models of asthenospheric flow assuming pressure, temperature, and stress-dependent viscosity show that ridge migration gives rise to small asymmetries in melt production rates of up to 5–11% for intermediate- to fast-spreading MORs[23]. Under reasonable assumptions of melt focusing, these models suggest that melt entrainment by adjacent ridge segments from this asymmetric melt production zone could readily account for the topographic changes reported here. These models also predict that depth anomalies across discontinuities should vary with ridge offset length, consistent with the observations.

The only available seismic studies of segment-scale variations in crustal thickness at fast ridges (NEPR 8° 30′–10° 30′ N) indicate slightly thinner crust (up to 300 m) at the trailing segment north of the Clipperton transform fault[8], consistent with our model. The much larger differences in crustal thickness (2–2.5 km) observed along ridge segments south of Clipperton[24] may reflect more local-scale processes (for example, the melt source for the Lamont seamounts and propagation history of the OSC). Gravity studies from other fast- and intermediate-spreading regions reveal along-axis variations in mantle Bouguer anomalies consistent with thinner crust (from a few hundred metres to ~1 km) at the trailing segments of both OSCs and transform faults[10,25,26]. In some of these locations, differences in inferred crustal thickness are much less than predicted

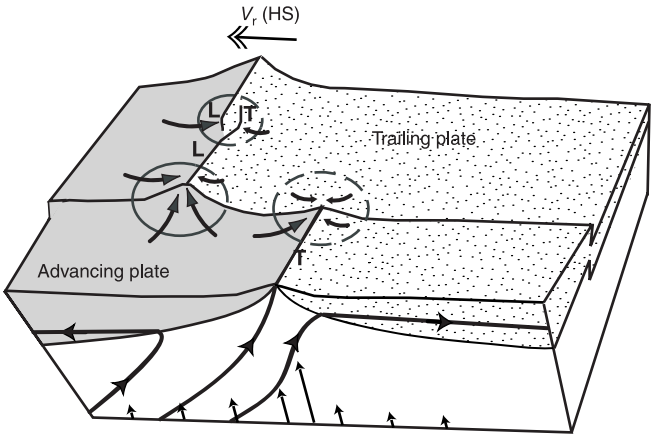

Figure 3 Schematic diagram illustrating asymmetric mantle upwelling beneath a migrating MOR offset at a transform fault and OSC. V_r (HS) indicates the velocity of ridge axis relative to the fixed 'hotspot' reference frame. Following refs 14 and 15, vertical mantle flow is proportional to the slope of the base of the lithosphere and the ridge-normal velocity of each plate with respect to the fixed mantle (vertical arrows). More rapid upwelling and greater melt production is predicted beneath an advancing plate. Stream lines show motion of asthenosphere relative to a stationary observer on the ridge, and indicate asymmetry in the path of mantle material beneath the two plates. The circles encompassing ridge segment ends illustrate idealized regions of mantle melt tapping which include the upwelling zone of the neighbouring segment across the discontinuity (solid/dashed line for advancing/trailing plate respectively, arrows show possible melt migration paths within zone). At leading segments (L), melt can be tapped from the more rapidly upwelling melt-rich zone of an advancing plate across a discontinuity, whereas trailing segments (T) draw melt from the less rapidly upwelling, less-melt-rich trailing plate. At OSCs the same process is envisaged, although probably confined to shallower mantle depths.

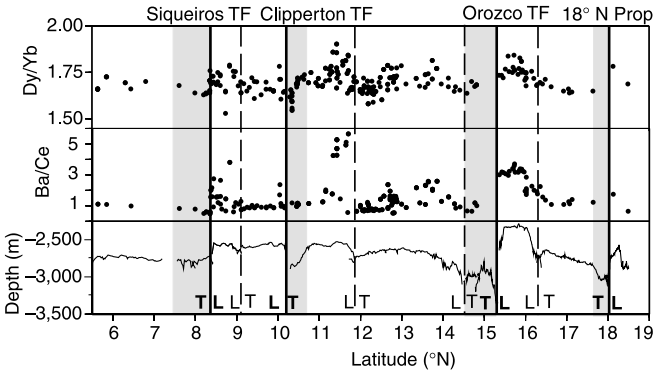

Figure 4 Axial depth and chemical parameters of zero-age lavas along the NEPR. Solid lines labelled in bold font mark large-offset discontinuities; dashed lines correspond to OSCs (offset >5 km). Labels identify leading (L) and trailing (T) segments across discontinuity. Grey shading highlights trailing segments at large-offset discontinuities. For this region, the most enriched and diverse compositions as indicated by incompatible element ratios Ba/Ce are associated with the shallow leading ridge segments. Higher Dy/Yb ratios, which indicate melt originating at greater mantle depths owing to the presence of residual garnet, are also associated with the leading segments. Data from refs 29, 30 and PetDB (http://petdb.ldeo.columbia.edu/petdb/). TF, transform fault.

for isostatically compensated topography (for example, assuming crustal densities of 2,700 kg m^{-3}, a 300-m difference in crustal thickness would only account for ~100 m of the depth change across the Clipperton tranform fault). Indeed, much of the difference in axial depth across discontinuities may be dynamic owing to thermal isostasy or viscous stresses, plausibly related to asymmetric mantle flow. Determining the relative contribution of dynamic forces versus differences in crustal thickness will require new studies of crustal and upper-mantle structure that target both leading and trailing segments.

The observed correlation between segment morphology and plate kinematics also provides a new framework within which geochemical variations along MORs can be evaluated. Geochemical differences in erupted lavas are observed across discontinuities, and are commonly attributed to melting of a veined mantle. Enriched veins are expected to begin to melt deeper in the mantle[27]. Our model provides a mechanism whereby these early-melting mantle heterogeneities within the upwelling zone of an adjacent advancing plate could be preferentially entrained beneath leading ridge segments. Along the NEPR, the most enriched and diverse lavas (as indicated by incompatible trace element ratios), as well as those derived from deepest melting, are found along leading segments (Fig. 4). As is typical elsewhere, geochemical studies along this ridge have focused on shallow segments believed to be magmatically robust, and inferences based on the existing data are subject to sampling bias. However, the currently available data for the NEPR are consistent with the notion that geochemical variability along this ridge may reflect the influence of plate kinematics on mantle melt production. Further evaluation of the geochemical implications of our model will require investigations of other areas that include targeted studies of the poorly sampled, trailing segments of MORs. □

Received 22 October 2003; accepted 13 May 2004; doi:10.1038/nature02652.

1. Macdonald, K. C. *et al.* A new view of the mid-ocean ridge from the behaviour of ridge-axis discontinuities. *Nature* **335,** 217–225 (1988).
2. Lin, J., Purdy, G. M., Schouten, H., Sempere, J.-C. & Zervas, C. Evidence from gravity data for focussed magmatic accretion along the Mid-Atlantic Ridge. *Nature* **344,** 627–632 (1990).
3. Cochran, J. R. & Sempere, J.-C. SEIR Scientific Team. The southeast Indian Ridge between 88°E and 118°E: gravity anomalies and crustal accretion at intermediate spreading rates. *J. Geophys. Res* **102,** 15463–15487 (1997).
4. Lin, J. & Phipps Morgan, J. The spreading rate dependence of three-dimensional mid-ocean ridge gravity structure. *Geophys. Res. Lett.* **19,** 13–16 (1992).
5. Wang, X., Cochran, J. R. & Barth, G. A. Gravity anomalies, crustal thickness, and the pattern of mantle flow at the fast spreading East Pacific Rise, 9°–10°N; evidence for three-dimensional upwelling. *J. Geophys. Res.* **101,** 17927–17940 (1996).
6. Langmuir, C. H., Bender, J. F. & Batiza, R. Petrological and tectonic segmentation of the East Pacific Rise, 5° 30′–14° 30′ N. *Nature* **322,** 422–429 (1986).
7. Detrick, R. S. *et al.* Multi-channel seismic imaging of a crustal magma chamber along the East Pacific Rise. *Nature* **326,** 35–41 (1987).
8. Van Adendonk, H. J. A., Harding, A. J., Orcutt, J. A. & McClain, J. S. Contrast in crustal structure across the Clipperton transform fault from travel time tomography. *J. Geophys. Res.* **106,** 10961–10981 (2001).
9. Scheirer, D. S. & Macdonald, K. C. Variation in cross-sectional area of the axial ridge along the East Pacific Rise; evidence for the magmatic budget of a fast spreading center. *J. Geophys. Res.* **98,** 7871–7885 (1993).
10. Cormier, M. H., Macdonald, K. C. & Wilson, D. S. A three-dimensional gravity analysis of the East Pacific Rise from 18° to 21° 30′S. *J. Geophys. Res.* **100,** 8063–8082 (1995).
11. The MELT Seismic Team, Imaging the deep seismic structure beneath a mid-ocean ridge: The MELT experiment. *Science* **280,** 1215–1218 (1998).
12. Stein, S., Melosh, H. J. & Minster, J. B. Ridge migration and asymmetric sea-floor spreading. *Earth Planet. Sci. Lett.* **36,** 51–62 (1977).
13. Small, C. & Danyushevsky, L. V. Plate-kinematic explanation for mid-oceanic-ridge depth discontinuities. *Geology* **31,** 399–402 (2003).
14. Davis, E. E. & Karsten, J. L. On the cause of the asymmetric distribution of seamounts about the Juan de Fuca Ridge; ridge-crest migration over a heterogeneous asthenosphere. *Earth Planet. Sci. Lett.* **79,** 385–396 (1986).
15. Schouten, H., Dick, H. J. B. & Klitgord, K. D. Migration of mid-ocean-ridge volcanic segments. *Nature* **326,** 835–839 (1987).
16. Madge, L. S. & Sparks, D. W. Three-dimensional mantle upwelling, melt generation, and melt migration beneath segment slow spreading ridges. *J. Geophys. Res.* **102,** 20571–20583 (1997).
17. Kent, G. M. *et al.* Evidence from three-dimensional seismic reflectivity images for enhanced melt supply beneath mid-ocean-ridge discontinuities. *Nature* **406,** 614–618 (2000).
18. Forsyth, D. W., Webb, S. C., Dorman, L. M. & Shen, Y. Phase velocities of Rayleigh waves in the MELT experiment on the East Pacific Rise. *Science* **280,** 1235–1238 (1998).
19. Toomey, D. R., Wilcock, W. S. D., Solomon, S. C., Hammond, W. C. & Orcutt, J. A. Mantle seismic structure beneath the MELT region of the East Pacific Rise from P and S wave tomography. *Science* **280,** 1224–1227 (1998).
20. Wolfe, C. J. & Solomon, S. C. Shear-wave splitting and implications for mantle flow beneath the MELT region of the East Pacific Rise. *Science* **280,** 1230–1232 (1998).
21. Conder, J. A., Forsyth, D. W. & Parmentier, E. M. Asthenospheric flow and asymmetry of the East Pacific Rise, MELT area. *J. Geophys. Res.* **107** doi:10.1029/2001JB000807 (2002).
22. Toomey, D. R. *et al.* Asymmetric mantle dynamics in the MELT region of the East Pacific Rise. *Earth Planet. Sci. Lett.* **200,** 287–295 (2002).
23. Katz, R., Spiegelman, M. & Carbotte, S. M. Ridge migration, asthenospheric flow and the origin of magmatic segmentation in the global mid-ocean ridge system. *Geophys. Res. Lett.* (submitted).
24. Canales, J. P., Detrick, R. S., Toomey, D. R. & Wilcock, W. S. D. Segment-scale variations in crustal structure of 150- to 300-k.y.-old fast spreading oceanic crust (East Pacific Rise, 8°15′N-10°15′N) from wide-angle seismic refraction profiles. *Geophys. J. Int.* **152,** 766–794 (2003).
25. Weiland, C. M. & Macdonald, K. C. Geophysical study of the East Pacific Rise 15° N-17° N; an unusually robust segment. *J. Geophys. Res.* **101,** 20257–20273 (1996).
26. Hooft, E. E. E. & Detrick, R. S. Relationship between axial morphology, crustal thickness, and mantle temperature along the Juan de Fuca and Gorda ridges. *J. Geophys. Res.* **100,** 22499–22508 (1995).
27. Hirschmann, M. M. & Stolper, E. W. A possible role for garnet pyroxenite in the origin of the "garnet signature" in MORB. *Contrib. Mineral. Petrol.* **124,** 185–208 (1996).
28. Gripp, A. E. & Gordon, R. G. Young tracks of hotspots and current plate velocities. *Geophys. J. Int.* **150,** 321–361 (2002).
29. Donnelly, K. E. *The Genesis of E-MORB: Extensions and Limitations of the Hot Spot Model.* Thesis, Columbia Univ. (2002).
30. Su, Y.-J. *Mid-ocean Ridge Basalt Trace Element Systematics: Constraints from Database Management, ICPMS Analyses, Global Data Compilation, and Petrologic Modeling*. Thesis, Columbia Univ. (2002).

Supplementary Information accompanies the paper on **www.nature.com/nature**.

Acknowledgements We thank R. Katz, M. Spiegelman, R. Buck and W.B.F. Ryan for discussions during the development of these ideas. Special thanks are due to W. Haxby for GeoMapApp, which greatly aided the data analysis. This work was supported by the US National Science Foundation, the Palisades Geophysical Institute, and the Doherty Foundation.

Competing interests statement The authors declare that they have no competing financial interests.

Correspondence and requests for materials should be addressed to S.M.C. (carbotte@ldeo.columbia.edu).

Radiocarbon evidence of mid-Holocene mammoths stranded on an Alaskan Bering Sea island

R. Dale Guthrie

Institute of Arctic Biology, University of Alaska, Fairbanks, Alaska 99775, USA

Island colonization and subsequent dwarfing of Pleistocene proboscideans is one of the more dramatic evolutionary and ecological occurrences[1–3], especially in situations where island populations survived end-Pleistocene extinctions whereas those on the nearby mainland did not[4]. For example, Holocene mammoths have been dated from Wrangel Island in northern Russia[4]. In most of these cases, few details are available about the dynamics of how island colonization and extinction occurred. As part of a large radiocarbon dating project of Alaskan mammoth fossils, I addressed this question by including mammoth specimens from Bering Sea islands known to have formed during the end-Pleistocene sea transgression[5]. One date of 7,908 ± 100 yr BP (radiocarbon years before present) established the presence of Holocene mammoths on St Paul Island, a first Holocene island record for the Americas. Four lines of evidence—265 accelerator mass spectrometer (AMS) radiocarbon dates from Alaskan mainland mammoths[6], 13 new dates from Alaskan island mammoths, recent reconstructions of bathymetric plots[5] and sea transgression rates from the Bering Sea[5]—made it possible to reconstruct how mammoths became stranded in the Pribilofs and why this apparently did not happen on other Alaskan Bering Sea islands.